

Non-Hermitian band topology in active and dissipative mechanical metamaterials

Colin Scheibner,^{1,2} William T. M. Irvine,^{1,2,3} and Vincenzo Vitelli^{1,2,*}

¹*James Franck Institute, The University of Chicago, Chicago, Illinois 60637, USA*

²*Department of Physics, The University of Chicago, Chicago, Illinois 60637, USA*

³*Enrico Fermi Institute, The University of Chicago, Chicago, Illinois, 60637, USA*

Networks of masses with transverse spring-like interactions provide a simple model of solids with energetic gain and loss. In this Letter, we study the non-Hermitian band topology of this model, which applies not only to active solids but also to gyroscopic metamaterials with dissipation. We examine a family of lattices in which topologically charged bands arise as activity (dissipation) is increased (decreased). The topological transition proceeds by a mechanism absent in Hermitian systems: Dirac cones spread out into exceptional rings rather than acquiring a gap. Above the transition, we observe chiral edge modes with a penetration depth that does not diverge even when the band gap closes.

Networks of masses connected by Hookean springs are a minimal, but surprisingly successful, model of solid materials. However, active solids, which possess energetic gain and loss, do not fit within this framework. A non-conservative generalization of Hookean springs was recently introduced in which the restoring force makes an angle θ with the bond [1], see Fig. 1a-c. Here, we use such active springs to study topological mechanical metamaterials, which are artificial structures possessing robust mechanical properties linked to the existence of topological invariants [2–17].

An intriguing feature of topological metamaterials with energetic gain and loss is that they can display a non-Hermitian dynamical matrix [1, 18, 19]. Topological metamaterials undergo transitions between different values of the topological indices when certain system parameters are varied [20, 21]. In this Letter, we investigate a class of non-Hermitian topological transitions in which θ is used as a control parameter for energetic gain vs. loss. The transition is mediated by the annihilation of exceptional rings, a mechanism absent in Hermitian counterparts. Moreover, we observe that the penetration depth of the edge modes does not diverge as the band gap closes.

Gain and loss via transverse forces— We begin by reviewing the role of transverse interactions in active solids [1]. To understand the connection between transverse forces and energetic gain and loss, first consider the dynamics of a single bond. In 2D, the most general linear pairwise force law that conserves linear momentum and depends only on the length of the bond may be written as [1]:

$$\mathbf{F}(\mathbf{r}) = -k\hat{\mathbf{n}}_\theta\delta r, \quad (1)$$

where k is the stiffness, $\hat{\mathbf{n}}_\theta$ is the unit vector forming an angle θ with the bond vector, $\delta r \equiv r - r_0$ is the deviation from the rest length r_0 , see Fig. 1a-c and S.I. The limiting case $\theta = 0$ corresponds to a standard Hookean spring.

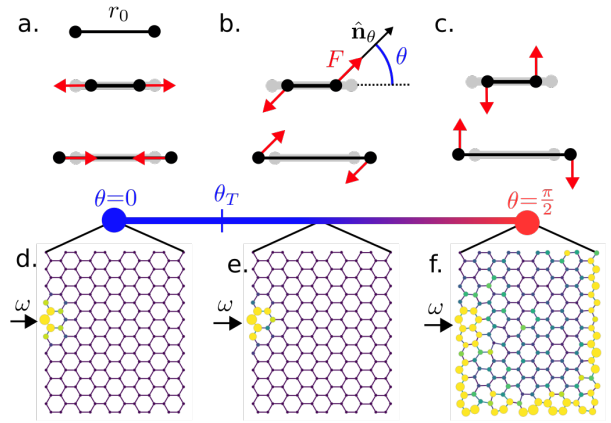


FIG. 1. Topological waves via non-reciprocal, active bonds. **a-c.** A family of active bonds parameterized by an angle θ between the bond vector and the restoring force. When $\theta = 0$, the bond is a standard Hookean spring whose restoring force (red) is directed along the bond vector (black). When $\theta = \pi/2$, the force is perpendicular to the bond vector. **d-e.** The bonds are placed on a network of massive nodes with free boundaries and overdamped dynamics. A single node is manually vibrated at a fixed frequency ω . The size and color of the nodes indicate the velocity of the particle. A topologically charged band-gap opens at $\theta_T = \pi/6$.

By contrast, the $\theta = \pi/2$ case gives a purely transverse interaction whereby clockwise (or counterclockwise) torques are generated when the bond is compressed (or stretched). One can easily see that θ acts a proxy for activity by evaluating $\nabla \times \mathbf{F} = k \sin(\theta)$ for small displacements. When brought on an infinitesimal quasistatic strain cycle, the active bond does positive (or negative) work given by $k \sin(\theta) \times A$, where A is the signed area enclosed by the relative coordinate \mathbf{r} along the cycle. Notably, for $\theta \neq 0$, the force law is chiral, i.e. violates parity, and entails sources of angular momentum [22]. We examine the overdamped dynamics given by

$$\Gamma \partial_t \mathbf{u} = \mathbf{F}, \quad (2)$$

which provides the dissipation needed to balance the ac-

* vitelli@uchicago.edu

tivity of \mathbf{F} .

Connection to gyroscopic metamaterials with loss — At first sight, active solids with non-conservative interactions have little to share with gyroscopic lattices whose Lagrangian dynamics can be derived from a potential. Nonetheless, the dynamics of the gyroscopes is modelled precisely by Eqs. (1-2) with $\theta = 0$. Moreover, with $\theta \neq 0$, these equations account for the hitherto neglected case of gyroscopes with dissipation. Consider two gyroscopes whose tips are connected by a Hookean spring so that the restoring force acts radially between them. The velocity of the tip of a fast spinning gyroscope, unlike that of an overdamped mass, is not proportional to the force. Instead, the torque, which is transverse to the radial force, determines the velocity of the tip [23, 24]. Consequently, the overdamped dynamics of active bonds with $\theta = \pi/2$ can be mathematically mapped onto the inertial dynamics of coupled gyroscopes, see S.I. This mapping is achieved by replacing \mathbf{F} with the in-plane components of torque and \mathbf{u} with the in-plane deflections of the gyroscopes. A hint of this connection emerges from considering the dynamics of a single overdamped bond obeying Eq. (1). When the bond of rest length $r_0 = 0$ is stretched and released, it spirals inward with angular frequency ω_0 and decay time τ_0 such that $\tau_0\omega_0 = \tan\theta$. At $\theta = \pi/2$, the lifetime τ_0 becomes infinite, which suggests a connection to conservative rotational dynamics. Upon plugging $\theta \neq \pi/2$ in Eq. (1), one obtains a description of gyroscopic dynamics with the addition of dissipation.

When $\theta = \pi/2$, it is known that a lattice of such gyroscopes forms a mechanical Chern insulator [23, 24]. Such a Chern insulator must necessarily violate a combination of classical time reversal symmetry (TSR) and parity [23, 25]. In our system, the left-hand side of Eq. (2) provides the TSR violation, and is not affected by varying θ . By contrast, the transverse components of the force in Eq. (1) are responsible for the parity violation and the angle θ sets their relative intensity.

Non-Hermitian lattice dynamics— Figure 1d-f shows snapshots from three separate simulations in which we place the active bonds on a honeycomb lattice and vibrate a particle on the edge at a fixed frequency. As the parameter θ is varied, we see how altering the balance between gain and loss affects the vibrational dynamics. At $\theta = 0$, no waves propagate while at $\theta = \pi/2$, an edge mode propagates indefinitely and unidirectionally. This persistent edge mode is ensured by the presence of a nonzero Chern number in the bulk spectrum. Yet, at $\theta = 0$, the system is a topologically trivial lattice of overdamped springs. Thus, in between these two limits, a topological transition must occur.

To understand this evolution, we cast the equation of motion for the unbounded lattice in terms of Fourier modes:

$$\mathbf{F}(\mathbf{q}, t) = -iH(\mathbf{q})\mathbf{u}(\mathbf{q}, t), \quad (3)$$

where \mathbf{u} is the displacement field, \mathbf{F} is the force which

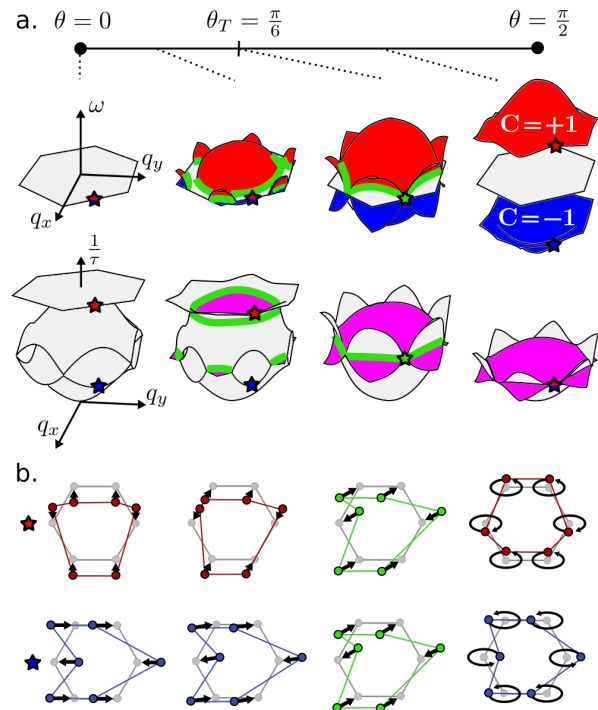


FIG. 2. Non-Hermitian topological transition and exceptional rings. **a.** The spectrum of the honeycomb lattice as a function of θ . The top row represents the oscillation frequency ω and the bottom row represents relaxation time $1/\tau$. Exceptional rings are highlighted in green. The red and blue regions indicate areas of highly positive (red) and negative (blue) Berry curvature. Above $\theta = \pi/6$, the spectrum contains two topologically charged bands with Chern numbers $C = \pm 1$. The purple in the top row represents degeneracies in the relaxational part of the red and blue bands. The spectrum contains an identically zero band omitted for clarity. **b.** The eigenmodes corresponding to the red and blue stars in the spectrum. The colored points represent the (exaggerated) eigenmode displacements. The black arrows indicate the path taken in time. At $\theta = \pi/6$ the eigenmodes become degenerate.

determines the time-evolution of \mathbf{u} , and $H(\mathbf{q})$ is a matrix [related to the dynamical matrix, $D(\mathbf{q})$, via $D(\mathbf{q}) = iH(\mathbf{q})$]. The Hermiticity of $H(\mathbf{q})$ encodes the intuitive notion of gain and loss [26–28]: $H(\mathbf{q})$ is Hermitian if and only if $|\mathbf{u}|^2$ is preserved in time. As θ evolves from 0 to $\pi/2$, the matrix $H(\mathbf{q})$ (when restricted to its optical modes) interpolates between being anti-Hermitian to Hermitian. As we show below, the non-Hermiticity of $H(\mathbf{q})$ plays a central role in the mechanism which mediates the topological transition.

A non-Hermitian topological transition— We now elucidate the differences between the transition shown in Fig. 1 and topological transitions in systems that remain Hermitian as their parameters are varied. Recall, for an isolated band in the bulk spectrum, the Chern number represents the total amount of Berry curvature over

the full Brillouin zone [29]. Topological transitions can only occur when two bands meet and the Berry curvature flows between them. In a Hermitian system, this degeneracy takes place at localized band crossings, such as Dirac cones. The emergence of a gap at these isolated points marks the onset of the topological transition.

In contrast to the Hermitian systems, the topological transition induced by the active bonds takes a different route. We first parse the non-Hermiticity of $H(\mathbf{q})$ into two distinct phenomena: (i) the eigenvalues become non-real, and (ii) the eigenvectors become non-orthogonal. As regards (i), the complex evolution of the spectrum is shown in Fig. 2a. The gradual decay of the imaginary (relaxational) part ($1/\tau$) paired with the growth of the real (propagating) part (ω) accounts for the emergence of propagating waves, but does not encode by itself a change of topology. Indeed, this change cannot account for the collective confinement to the edge because it can be rationalized at the level of a single bond: the quantity $\tau\omega_0 = \tan\theta$ tends to infinity as energy is injected at each wave cycle that offsets the dissipation.

Mechanism of the transition— From a topological perspective, the more substantial change is the evolution of the eigenvectors. The leftmost column of Fig. 2b shows two eigenvectors of $H(\mathbf{q})$, i.e. normal modes, when $\theta = 0$. In this dissipative limit, the normal modes are mutually orthogonal, like those in a Hermitian system. When θ increases, the orthogonality is lost and the eigenmodes, as shown in the second column, begin to mix. As the evolution progresses, the mixing results in an extreme situation in which two or more eigenvectors coalesce. This intrinsically non-Hermitian occurrence, called an *exceptional point* [30–36], takes place along the rings highlighted in green in Fig. 2a. In the third column of Fig. 2b, we show how the two highlighted eigenvectors align as an exceptional ring passes through their location in the Brillouin zone. After the exceptional ring passes, the modes obtain a circulating character that enables propagation, i.e. nonzero ω .

These exceptional rings mediate the flow of Berry curvature necessary for a topological transition. At $\theta = 0$, the spectrum is pierced by Dirac cones at the center and corners of the Brillouin zone, shown in Fig. 2a. These Dirac cones initially act as monopoles of Berry curvature [37]. When θ increases, however, the Dirac cones do not simply acquire a gap, as would be typical in Hermitian systems. Instead, they spread out into exceptional rings that enclose regions of highly positive and negative Berry curvature, indicated, respectively, by the red and blue regions in Fig. 2a.

A band gap cannot spontaneously emerge along a single isolated exceptional ring since the two participating bands share a single eigenvector. At $\theta_T = \pi/6$, however, the two exceptional rings collide and annihilate, allowing a band gap to open. During the gap-opening, previously isolated regions with the same sign of Berry curvature connect, thus producing two separable bands with nonzero topological charge. We emphasize that

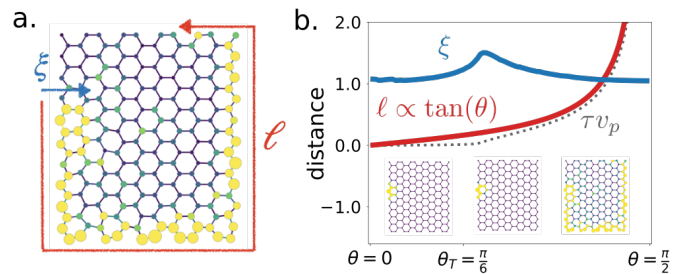


FIG. 3. **Competing length scales and non-divergent penetration depth.** **a.** Two distinct length scales characterize the topological edge modes: the penetration depth ξ and the propagation distance ℓ . **b.** These length scales are computed numerically (see S.I.) and plotted as a function of θ . We note that the penetration depth (blue) does not diverge even when the band gap closes at $\theta_T = \pi/6$. The propagation distance ℓ (in grey) is computed via the quantity τv_p , where τ is the lifetime and v_p is the phase velocity. This length scale is well characterized by the property of a single bond $\tau\omega_0 = \tan(\theta)$. All lengths are in units of the lattice spacing.

this mechanism of topological transition, namely exceptional ring annihilation, crucially relies on $H(\mathbf{q})$ being non-Hermitian. The exceptional rings can only exist in non-Hermitian systems because they represent lines at which the matrix $H(\mathbf{q})$ is defective [31, 33, 35, 38–53].

Origin of non-Hermiticity: geometry of nonconservative interactions— The transition we observe is enabled by a geometric origin of non-Hermiticity that differs from generic dissipation or activity. To contrast, there is a sense in which even conventional solids and fluids are described non-Hermitian operators. Friction and viscosity, for example, give rise to attenuation of waves. The model we study here falls within a specialized class of continuum media with loss or gain. Crucially, we note that the energetic gain and loss in the transformation illustrated in Fig. 1 is encoded in the spatial geometry of the interactions, and not in the dynamics. For example, one could imagine tuning gain and loss by adding (isotropic) dissipation Γ to an inertial system with standard Hookean springs, e.g. $m\partial_t^2\mathbf{u} + \Gamma\partial_t\mathbf{u} = \mathbf{F}_{\theta=0}$. In this case, tuning Γ alone would not induce a topological transition. The key reason is that varying Γ would only lead to attenuation of the normal modes, i.e. only their amplitude changes. In our system, activity or dissipation enters the spatial geometry of the force law, not its rate dependence. As a consequence, varying θ changes the normalized modes themselves (c.f. Fig. 2b), thus enabling a change in topology.

Characteristic length scales— Here we elucidate the behavior of two characteristic length scales that differentiate our system from standard mechanical Chern insulators [23, 54, 55]. The first length scale, shown in Fig. 3a, is the propagation distance ℓ of the edge mode along the system’s boundary. We quantify ℓ by computing τv_p where τ is the lifetime and $v_p = \omega/q$ is the phase velocity, plotted in grey in Fig. 3b. We note that ℓ arises

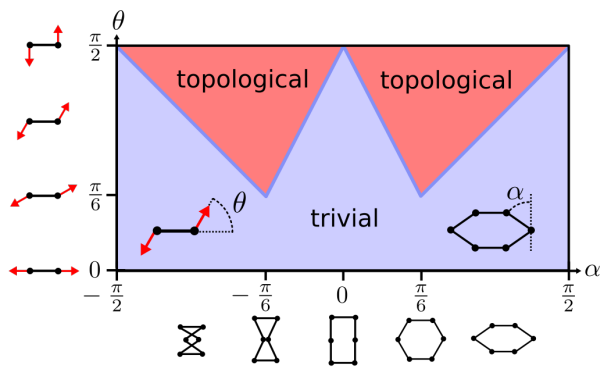


FIG. 4. **Activity threshold and lattice geometry.** A phase diagram for topology in terms of lattice geometry and interaction geometry. The angle α parameterizes the family of deformed honeycomb lattices, while θ characterizes the gain and loss in the bonds.

from the competition of two time scales (ω and τ) and is therefore determined entirely by the eigenvalues, not the eigenvectors, of $H(\mathbf{q})$. As a result, the qualitative behavior of ℓ is well captured by the quantity $t_0\omega_0 = \tan(\theta)$, indicating that the general ability to propagate results from the balance of gain and loss within a single bond. For an ideal Hermitian system $\ell = \infty$ since there is no source of gain nor loss.

The second crucial length scale is the penetration depth ξ of the edge mode *into* the bulk. Unlike ℓ , the quantity ξ is a property of the eigenvectors of $H(\mathbf{q})$ only and not of its eigenvalues. The penetration depth for a wide class of Chern insulators typically diverges when the band gap closes as the topological edge modes assimilate into the bulk [56]. By contrast, in Fig. 3b, we plot ξ as a function of θ (blue) and note that ξ remains approximately constant even when the topological transition occurs at $\theta_T = \pi/6$. This is reminiscent of the topological transition between $C = 1$ and $C = -1$ that occurs in the inversion-symmetric Haldane model [57]. In that case, the penetration depth does not diverge as the second-neighbor hopping phase is tuned through the graphene point. As in the system we study, the crucial feature is that localized edge modes (topological or not) exist on both sides of the transition. This allows for a continuous interpolation between the two states without a divergence of the penetration depth.

Even though the edge mode remains confined to the boundary below $\theta_T = \pi/6$, the mode only begins to propagate above the topological transition, as can be seen by the sharp kink in the grey τv_p curve. The markedly different behavior between ℓ and ξ speaks to the difference between their physical origins. The quantity ℓ arises from the balance between energetic gain and loss in a single bond. By contrast, ξ results from the interplay between the lattice geometry and the geometry of the nonconservative interactions.

Modulating activity threshold via zero-mode deformations — One of the unique features of the nonconservative

bond described by Eq. (1) is that the activity (or dissipation) enters through a geometric quantity: the angle θ . The onset of topology in this system is therefore independent of temporal information and depends instead on the interplay between lattice geometry and the geometry associated with the nonconservative forces. To explore this interplay, the phase diagram in Fig. 4 shows how zero-mode deformations of the underlying honeycomb lattice modulate the critical value θ_T at which the gap opens. We parameterize the geometry of the unit cell via the angle α shown in Fig. 4. Previous studies on gyroscopic metamaterials have probed the dissipationless line $\theta = \pi/2$ and revealed that topology is inaccessible at $\alpha = 0, \pm\pi/2$ [20]. However, as we look below $\theta = \pi/2$, we find that for any value of α , there is always a finite range of θ for which the system is topologically trivial. This feature of the phase diagram can be inferred from the non-Hermitian topological mechanism discussed above: since the exceptional points have to travel a finite distance across the Brillouin zone to annihilate, there must be a finite range of θ for which the system is topological trivial.

By lifting the constraint of energy conservation in active and dissipative metamaterials, we uncover topological transitions that are controlled by the interplay between nonconservative interactions, dissipation and lattice geometry. The mechanism behind these transitions is the spreading of Dirac cones into exceptional rings as activity (dissipation) increases (decreases). Additionally, the chiral edge mode in the systems we study displays a penetration depth that, unlike typical Chern insulators, does not diverge as the band gap closes.

Acknowledgements V.V. was supported by the Complex Dynamics and Systems Program of the Army Research Office under grant W911NF-19-1-0268. W.T.M.I. and VV acknowledge support through the Chicago MRSEC, funded by the NSF through grant DMR-1420709. C.S. was supported by the National Science Foundation Graduate Research Fellowship under Grant No. 1746045. W.T.M.I. acknowledges support from NSF EFRI NewLAW grant 1741685 and NSF DMR 1905974. We would like to thank A. Souslov and M. Fruchart for stimulating and helpful discussions.

I. SUPPLEMENTARY INFORMATION

A. Transverse interactions

1. Active bond

In the main text, we present the pairwise interaction from Ref. [1]:

$$\mathbf{F} = -k\hat{\mathbf{n}}_\theta\delta r, \quad (\text{S1})$$

where k is the stiffness, $\hat{\mathbf{n}}_\theta$ is the unit vector rotated by an angle θ with respect to the bond vector, and $\delta r = r - r_0$ is the displacement from its equilibrium separation r_0 , see Fig. 1 in the main text for an illustration. The vector $\hat{\mathbf{n}}_\theta$ can be written in terms of the bond vector $\hat{\mathbf{r}}$ as:

$$\begin{pmatrix} \hat{n}_x \\ \hat{n}_y \end{pmatrix} = \begin{pmatrix} \cos\theta & \sin\theta \\ -\sin\theta & \cos\theta \end{pmatrix} \begin{pmatrix} \hat{r}_x \\ \hat{r}_y \end{pmatrix}. \quad (\text{S2})$$

Here, we show that Eq. (S1) is the most general 2D pairwise interaction subject to the following conditions:

- (i) The interaction only depends on the distance between the particles.
- (ii) The interaction conserves linear momentum.
- (iii) The interaction is linear in its displacements from an equilibrium length r_0 .

For a 2D interaction obeying property (i), it is sufficient to specify the forces $\mathbf{F}_1(r)$ and $\mathbf{F}_2(r)$ on the two participating particles as a function of their separation r . Condition (ii) implies that $\mathbf{F}_1(r) = -\mathbf{F}_2(r)$, so it is sufficient to specify a single function $\mathbf{F}(r)$. By assumption (iii), we may write $\mathbf{F}(r) = \mathbf{k}\delta r$, where \mathbf{k} is a 2D vector and $\delta r = r - r_0$ is the displacement from mechanical equilibrium. By parameterizing \mathbf{k} as $\mathbf{k} = k\hat{\mathbf{n}}_\theta$, we obtain Eq. (S1). We note that such a bond with overdamped dynamics $\Gamma\partial_t\mathbf{u} = \mathbf{F}$ is only dynamically stable when

$$\Gamma k \cos(\theta) \geq 0. \quad (\text{S3})$$

Without loss of generality, we explore the stable range of parameters $k, \Gamma \geq 0$ and $\theta \in [-\pi/2, \pi/2]$.

2. Mapping to dissipative gyroscopic metamaterials

Now we show how the active force law in Eq. (S1) can be mapped onto the dynamics of a gyroscopic metamaterial with dissipation. We consider a system of gyroscopes suspended vertically with their bases fixed and free ends connected by Hookean springs, similar to those studied in Refs. [20, 21, 24, 58, 59]. In the fast spinning limit, the angular momentum of the gyroscope is given by $\mathbf{L} = \Omega I \hat{\boldsymbol{\ell}}$, where Ω and I are, respectively, the angular velocity and moment of inertia about the axis of

the gyroscope $\hat{\boldsymbol{\ell}}$. When a force \mathbf{F} is applied to the free tip, the gyroscope experiences a torque

$$\boldsymbol{\tau} = \ell \mathbf{F} \times \hat{\boldsymbol{\ell}} \quad (\text{S4})$$

about its fixed base, where ℓ is the length of the gyroscope. We have assumed for simplicity that the center of mass of the gyroscope coincides with the point at which the force acts. Hence, we obtain the equation of motion:

$$\Omega I \partial_t \hat{\boldsymbol{\ell}} = \partial_t \mathbf{L} \quad (\text{S5})$$

$$= \boldsymbol{\tau} \quad (\text{S6})$$

$$= \ell \mathbf{F} \times \hat{\boldsymbol{\ell}}. \quad (\text{S7})$$

We will now use a Cartesian coordinate system in which the $\hat{\mathbf{z}}$ is oriented vertically, parallel to the rest orientation of the gyroscopes. For small deflections from vertical, we may write the in-plane displacements of the tip as $u_x = \ell \hat{\ell}_x$ and $u_y = \ell \hat{\ell}_y$. When two gyroscopes are connected by Hookean springs, such that the spring is at its rest length r_0 when the gyroscopes are vertical, the in-plane spring forces to leading order in u_i are given by:

$$F_i^s = k \hat{n}_i \delta r, \quad (\text{S8})$$

where the indices run over x and y , \hat{n}_i is the in-plane bond vector, and $\delta r = r - r_0$ is the change in spring length. We note that geometric nonlinearities, such as out-of-plane motion of the spring, are subleading in u_i . In addition to the spring force, we consider a dissipative drag term that takes the form:

$$F_i^d = -\gamma \partial_t u_i. \quad (\text{S9})$$

Combining Eqs. (S7-S9), the in-plane equations of motion to leading order in u_i become:

$$\frac{\Omega I}{\ell} \partial_t u_i = k \epsilon_{ij} \hat{n}_j \delta r - \gamma \epsilon_{ij} \partial_t u_j. \quad (\text{S10})$$

Now we define

$$\Gamma = \sqrt{\left(\frac{\Omega I}{\ell}\right)^2 + \gamma^2} \quad (\text{S11})$$

$$\hat{n}_{\theta i} = \left(\frac{\Omega I}{\Gamma \ell} \epsilon_{ik} + \frac{\gamma}{\Gamma} \delta_{ik}\right) \hat{n}_k. \quad (\text{S12})$$

We note that \hat{n}_θ in Eq. (S12), is simply the vector \hat{n}_i rotated through the angle $\theta = \arctan\left(\frac{\Omega I}{\gamma \ell}\right)$. Using the definitions of Γ and $\hat{n}_{\theta i}$, Eq. (S10) takes the form:

$$\Gamma \partial_t u_i = k \hat{n}_{\theta i} \delta r, \quad (\text{S13})$$

which is mathematically homomorphic to the overdamped active bond studied in Ref. [1]. Notice, however, that the gyroscopic system is not active, since it consists of a passive, inertial system of gyroscopes with added dissipation. The righthand side of Eq. (S13) should *not* be interpreted as a physical force, but rather a subset of the total torque that governs the evolution of the angular momentum parameterized by u_i . We note that when the dissipation vanishes, $\gamma = 0$, equation Eq. (S13) goes to the $\theta = \pi/2$ limit and describes a system for which energy is conserved.

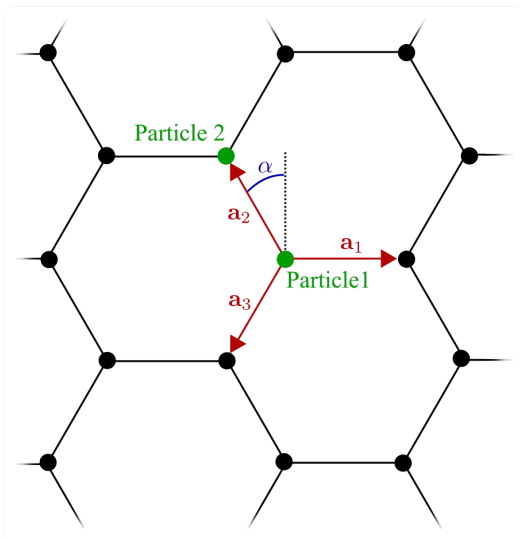


FIG. S1. **Notation for honeycomb lattice calculation.** An illustration the symbols defined in the text. The unit cell consists of two particles: particle-1(2) corresponds to displacements and forces denoted by $\mathbf{u}_{1(2)}$ and $\mathbf{F}_{1(2)}$, respectively.

B. Spectrum calculations

In this section, we compute the spectrum and Berry curvature displayed in Fig. 2, as well as the phase diagram shown in Fig. 4. in the main text. Throughout, we will rescale all lengths by the lattice spacing of the undeformed honeycomb lattice, and we will set $k = \Gamma = 1$, where k is the spring constant and Γ is the drag coefficient appearing in the overdamped equation of motion $\Gamma \partial_t \mathbf{u} = \mathbf{F}$. This is equivalent to rescaling all frequencies by k/Γ .

1. Expression for $H(\mathbf{q})$

We begin by deriving an expression for $H(\mathbf{q})$ for the family of deformed Honeycomb lattices. As illustrated in Fig. S1, the unit cell consists of two particles and three bond vectors given by:

$$\mathbf{a}_1 = a \begin{pmatrix} 1 \\ 0 \end{pmatrix} \quad (\text{S14})$$

$$\mathbf{a}_2 = a \begin{pmatrix} -\sin \alpha \\ \cos \alpha \end{pmatrix} \quad (\text{S15})$$

$$\mathbf{a}_3 = a \begin{pmatrix} -\sin \alpha \\ -\cos \alpha \end{pmatrix}, \quad (\text{S16})$$

where $a = \frac{1}{\sqrt{3}}$ is the bond length.

Let $\mathbf{u}_1(\mathbf{x})$ and $\mathbf{u}_2(\mathbf{x})$ denote the displacements of particles 1 and 2, respectively, at position \mathbf{x} . Then the forces

$\mathbf{F}_1(\mathbf{x})$ and $\mathbf{F}_2(\mathbf{x})$ on these particles is given by

$$\mathbf{F}_1(\mathbf{x}) = R(\theta) \sum_i A_i [\mathbf{u}_2(\mathbf{x} + \mathbf{a}_i) - \mathbf{u}_1(\mathbf{x})] \quad (\text{S17})$$

$$\mathbf{F}_2(\mathbf{x}) = R(\theta) \sum_i A_i [\mathbf{u}_1(\mathbf{x} - \mathbf{a}_i) - \mathbf{u}_2(\mathbf{x})], \quad (\text{S18})$$

where

$$R(\theta) = \begin{pmatrix} \cos \theta & \sin \theta \\ -\sin \theta & \cos \theta \end{pmatrix} \quad (\text{S19})$$

$$A_1 = \hat{\mathbf{a}}_1 \otimes \hat{\mathbf{a}}_1 = \begin{pmatrix} 1 & 0 \\ 0 & 0 \end{pmatrix} \quad (\text{S20})$$

$$A_2 = \hat{\mathbf{a}}_2 \otimes \hat{\mathbf{a}}_2 = \begin{pmatrix} \sin^2 \alpha & -\sin \alpha \cos \alpha \\ -\sin \alpha \cos \alpha & \cos^2 \alpha \end{pmatrix} \quad (\text{S21})$$

$$A_3 = \hat{\mathbf{a}}_3 \otimes \hat{\mathbf{a}}_3 = \begin{pmatrix} \sin^2 \alpha & \sin \alpha \cos \alpha \\ \sin \alpha \cos \alpha & \cos^2 \alpha \end{pmatrix} \quad (\text{S22})$$

Notice that the $R(\theta)$ incorporates the effect of the non-conservative bonds. Taking the Fourier transformation of Eqs. (S17-S18) with the convention $f(\mathbf{x}) = \int \frac{d^2 q}{(2\pi)^2} f(\mathbf{q}) e^{i\mathbf{q}\cdot\mathbf{x}}$ yields the following expression for $H(\mathbf{q})$:

$$H(\mathbf{q}) = i \begin{pmatrix} -R(\theta) \sum_i A_i & R(\theta) \sum_i e^{i\mathbf{q}\cdot\mathbf{a}_i} A_i \\ R(\theta) \sum_i e^{-i\mathbf{q}\cdot\mathbf{a}_i} A_i & -R(\theta) \sum_i A_i \end{pmatrix}. \quad (\text{S23})$$

To obtain the eigenvalues of $H(\mathbf{q})$, we solve the characteristic polynomial $P(\lambda) = \det[H(\mathbf{q}) - \lambda I]$, where I is the 4×4 identity matrix. Using the convention $f(t) = \int \frac{d\omega}{2\pi} f(\omega) e^{-i\omega t}$, the frequency of propagation associated with the eigenvalue λ is given by $\omega = \text{Re}(\lambda)$, and the decay time τ is given by $1/\tau = -\text{Im}(\lambda)$.

2. Honeycomb lattice spectrum

For the honeycomb lattice, we evaluate the characteristic polynomial at $\alpha = \pi/6$ and obtain:

$$p(\lambda) = \lambda \left\{ \lambda^3 - 6i\lambda^2 \cos \theta - \frac{\lambda}{2} [18 + G(2 \cos 2\theta - 1)] + i\frac{3}{2} G \cos \theta \right\}, \quad (\text{S24})$$

where all the \mathbf{q} dependence is captured in the θ -independent quantity:

$$G = 3 - \cos q_y - 2 \cos \frac{q_y}{2} \cos \frac{\sqrt{3}}{2} q_x. \quad (\text{S25})$$

Notice that the polynomial in Eq. (S24) has a trivial root $\lambda = 0$ that corresponds to a zero mode shearing of the lattice. After factoring out the zero mode, the remaining polynomial may be solved to produce the spectrum plots in Fig. 2a. To determine that the degeneracies in the spectrum are exceptional points, we check that the determinant of the matrix of eigenvectors vanishes at the locations of the degeneracies. We note that the location of the exceptional rings may be obtained by solving for the values G for which $p(\lambda)$ has repeated roots.

3. Topology onset for deformed honeycomb

Now we consider the deformed honeycomb lattice, for which $\alpha \neq \pi/6$. For $|\alpha| \leq \pi/6$ we numerically observe that the band gap opens at the point:

$$\begin{pmatrix} q_x \\ q_y \end{pmatrix} = \begin{pmatrix} \frac{\sqrt{3}\pi}{1+\sin\alpha} \\ 0 \end{pmatrix} \quad (\text{S26})$$

and the points equivalent by symmetry. The roots of the characteristic polynomial at these points are given by:

$$\lambda = 0 \quad (\text{S27})$$

$$\lambda = -i2 \cos \theta \quad (\text{S28})$$

$$\lambda = -i2 \cos \theta \pm i\sqrt{2(\cos 2\theta + \cos 4\alpha)}. \quad (\text{S29})$$

Hence, we find that the topological transition occurs at

$$\theta_T = \begin{cases} \pi/2 - 2\alpha & 0 < \alpha \leq \pi/6 \\ \pi/2 + 2\alpha & -\pi/6 \leq \alpha < 0. \end{cases} \quad (\text{S30})$$

Similarly, for $\pi/6 \leq |\alpha| \leq \pi/2$, we observe that the gap-opening occurs at

$$\begin{pmatrix} q_x \\ q_y \end{pmatrix} = \begin{pmatrix} \frac{\sqrt{3}\pi}{2(1+\sin\alpha)} \\ \frac{\sqrt{3}\pi}{2\cos\alpha} \end{pmatrix}, \quad (\text{S31})$$

and the points equivalent by symmetry. The roots at these points are given by:

$$\lambda = 0 \quad (\text{S32})$$

$$\lambda = -i2 \cos \theta \quad (\text{S33})$$

$$\lambda = -i2 \cos \theta \pm i\sqrt{2(\cos 2\theta - \cos 2\alpha)}, \quad (\text{S34})$$

which implies that the transition occurs at:

$$\theta_T = \begin{cases} \alpha & \pi/6 \leq \alpha \leq \pi/2 \\ -\alpha & -\pi/2 \leq \alpha \leq -\pi/6. \end{cases} \quad (\text{S35})$$

4. Calculation of Berry curvature

In Fig. 2 of the main text, the sign of the Berry curvature of the participating bands is indicated using color. The Berry curvature associated with the n th band of a Hermitian Hamiltonian of a 2D system is given by:

$$F(\mathbf{q}) = \epsilon_{ij} \frac{\partial A_j(\mathbf{q})}{\partial q_i}, \quad (\text{S36})$$

where $A_j(\mathbf{q})$ is the Berry connection, defined by

$$A_j(\mathbf{q}) = i \langle n(\mathbf{q}) | \frac{\partial}{\partial q_j} | n(\mathbf{q}) \rangle, \quad (\text{S37})$$

and $|n(\mathbf{q})\rangle$ is the eigenvector associated with the n th band, see, e.g. Ref. [60]. For a Hermitian operator H , the eigenvector $|n(\mathbf{q})\rangle$ obeys the definition

$$H |n\rangle = \lambda_n |n\rangle. \quad (\text{S38})$$

However, for a non-Hermitian operator, ambiguity arises in the definition of the eigenstate because the two vectors $|n_R\rangle$ and $|n_L\rangle$ defined by

$$H |n^R\rangle = \lambda_n |n^R\rangle \quad (\text{S39})$$

$$H^\dagger |n^L\rangle = \lambda_n^* |n^L\rangle \quad (\text{S40})$$

need not be equal. Following the approach in, e.g., Ref. [35], for a non-Hermitian system, one can define at least four different generalization of the Berry connection:

$$A_j^{RR}(\mathbf{q}) = i \langle n^R(\mathbf{q}) | \frac{\partial}{\partial q_j} | n^R(\mathbf{q}) \rangle \quad (\text{S41})$$

$$A_j^{RL}(\mathbf{q}) = i \langle n^R(\mathbf{q}) | \frac{\partial}{\partial q_j} | n^L(\mathbf{q}) \rangle \quad (\text{S42})$$

$$A_j^{LL}(\mathbf{q}) = i \langle n^L(\mathbf{q}) | \frac{\partial}{\partial q_j} | n^L(\mathbf{q}) \rangle \quad (\text{S43})$$

$$A_j^{LR}(\mathbf{q}) = i \langle n^L(\mathbf{q}) | \frac{\partial}{\partial q_j} | n^R(\mathbf{q}) \rangle. \quad (\text{S44})$$

Generically, each of these definitions will a different result for the local Berry curvature $F(\mathbf{q})$. However, regardless of which expression for $A_j(\mathbf{q})$ is used in Eq. (S36), the total Berry curvature of the band integrated over the full Brillouin zone (BZ) will be unchanged. Hence, the Chern number

$$C = \frac{1}{2\pi} \int_{BZ} d^2q F(\mathbf{q}). \quad (\text{S45})$$

is insensitive to the choice of connection. For our calculations, all four definition of $A_j(\mathbf{q})$ produce the result shown in Fig. 2, which is only sensitive to the sign of the Berry curvature. In practice, we compute the distribution of Berry curvature over each band using the numerical approach described in Ref. [61].

C. Numerics

1. Simulations

We now describe the simulations depicted in main-text Fig. 1. The simulations shown are performed on a lattice of 15 by 15 unit cells with free boundaries on all sides. The position of each particle is integrated according the following second-order Runge-Kutta scheme:

$$\mathbf{x}_i \left(t + \frac{1}{2} \Delta t \right) = \mathbf{x}_i(t) + \frac{1}{2} \Delta t \mathbf{F}_i[\mathbf{x}(t)] \quad (\text{S46})$$

$$\mathbf{x}_i(t + \Delta t) = \mathbf{x}_i(t) + \Delta t \mathbf{F}_i \left[\mathbf{x} \left(t + \frac{1}{2} \Delta t \right) \right], \quad (\text{S47})$$

where Δt is the time step, $\mathbf{x}_i(t)$ is the position of the i th particle, and \mathbf{F}_i is the force on the i th particle as determined by the interaction law and the list of other particle positions $\mathbf{x}(t)$. In our simulations, time is measured of

units of Γ/k and distances are measured in units of the lattice spacing.

The particles are initialized at their rest positions, and a single particle on the boundary of the lattice is subjected to controlled displacements given by $\mathbf{u}(t) = (A \cos(\omega t), 0)$. For the simulations shown, $A = 0.1$, $\omega = 0.5$, $\Delta t = 0.1$, and θ ranges over the values $\theta \in \{0, \pi/4, \pi/2\}$. The final time shown in the figure is $t_f = 100$ for the simulations with $\theta = 0, \pi/4$ and $t_f = 50$ for $\theta = \pi/2$.

2. Characterization of length scales

We now describe the numerical procedure for determining the length scales shown in Fig. 3. Using the notation of Fig. S1, we consider a system with $n = 30$ unit cells in the horizontal (x) direction and unbounded in the vertical (y) direction. Performing a Fourier transform with respect to the vertical coordinate gives rise to a Hamiltonian expressed as a $2n$ by $2n$ matrix of the form:

$$H(q_y) = i \begin{bmatrix} -\frac{3}{2}R & RB & & & & \\ RB^\dagger & -\frac{3}{2}R & RC & & & 0 \\ & RC^\dagger & -\frac{3}{2}R & RB & & \\ & & RB^\dagger & -\frac{3}{2}R & RC & \\ & & & RC^\dagger & \ddots & \\ 0 & & & & & \ddots & RB \\ & & & & & RB^\dagger & -\frac{3}{2}R \end{bmatrix}, \quad (\text{S48})$$

where

$$B = A_2 + e^{iq_y} A_3 \quad (\text{S49})$$

$$C = e^{i\frac{q_y}{2}} A_1, \quad (\text{S50})$$

with A_1, A_2, A_3 and R defined in Eqs. (S19-S22).

We numerically find the eigenvalues and eigenvectors of $H(q_y)$. We sort the eigenvectors by their localization, and we find that the edge modes are well characterized by the form $\mathbf{u}(\theta, q_y, x) \propto e^{-x/\xi(\theta, q_y)}$. In Fig. 3b, we plot ξ and ℓ as a function of θ at $q_y = \pi$.

-
- [1] Scheibner, C. *et al.* Odd elasticity (2019). arXiv:1902.07760.
 - [2] Mousavi, S. H., Khanikaev, A. B. & Wang, Z. Topologically protected elastic waves in phononic metamaterials. *Nature Communications* **6**, 8682 (2015).
 - [3] Susstrunk, R. & Huber, S. D. Observation of phononic helical edge states in a mechanical topological insulator. *Science* **349**, 47–50 (2015).
 - [4] Paulose, J., Chen, B. G.-g. & Vitelli, V. Topological modes bound to dislocations in mechanical metamaterials. *Nat Phys* **11**, 153–156 (2015).
 - [5] Paulose, J., Meeussen, A. S. & Vitelli, V. Selective buckling via states of self-stress in topological metamaterials. *Proceedings of the National Academy of Sciences* **112**, 7639–7644 (2015).
 - [6] Rocklin, D. Z., Zhou, S., Sun, K. & Mao, X. Transformable topological mechanical metamaterials. *Nature Communications* **8**, 14201 (2017).
 - [7] Chen, B. G. G. *et al.* Topological Mechanics of Origami and Kirigami. *Physical Review Letters* **116**, 135501 (2016).
 - [8] Susstrunk, R. & Huber, S. D. Classification of topological phonons in linear mechanical metamaterials. *Proceedings of the National Academy of Sciences* **113**, E4767–E4775 (2016).
 - [9] Chen, B. G.-g., Upadhyaya, N. & Vitelli, V. Nonlinear conduction via solitons in a topological mechanical insulator. *Proceedings of the National Academy of Sciences of the United States of America* **111**, 13004–13009 (2014).
 - [10] Meeussen, A. S., Paulose, J. & Vitelli, V. Geared topological metamaterials with tunable mechanical stability. *Phys. Rev. X* **6**, 041029 (2016).
 - [11] Guest, S. & Hutchinson, J. On the determinacy of repetitive structures. *Journal of the Mechanics and Physics of Solids* **51**, 383–391 (2003).
 - [12] Rocklin, D. Directional mechanical response in the bulk of topological metamaterials. *arXiv preprint arXiv:1612.00084* (2016).
 - [13] Bilal, O. R., Susstrunk, R., Daraio, C. & Huber, S. D. Intrinsically polar elastic metamaterials. *Advanced Materials* 1700540 (2017).
 - [14] Rocklin, D. Z., Zhou, S., Sun, K. & Mao, X. Transformable topological mechanical metamaterials. *Nature communications* **8**, 14201 (2017).
 - [15] Abbaszadeh, H., Souslov, A., Paulose, J., Schomerus, H. & Vitelli, V. Sonic Landau levels and synthetic gauge fields in mechanical metamaterials. *Phys. Rev. Lett.* **119**, 195502 (2017).
 - [16] Kane, C. L. & Lubensky, T. C. Topological boundary modes in isostatic lattices. *Nature Physics* **10**, 39–45

- (2014).
- [17] Sone, K. & Ashida, Y. Anomalous topological active matter. *Phys. Rev. Lett.* **123**, 205502 (2019).
- [18] Brandenbourger, M., Locsin, X., Lerner, E. & Coulais, C. Non-reciprocal robotic metamaterials. *Nature Communications* **10**, 4608 (2019).
- [19] Ghatak, A., Brandenbourger, M., van Wezel, J. & Coulais, C. Observation of non-hermitian topology and its bulk-edge correspondence (2019). arXiv:1907.11619v1.
- [20] Mitchell, N. P., Nash, L. M. & Irvine, W. T. M. Tunable band topology in gyroscopic lattices. *Phys. Rev. B* **98**, 174301 (2018).
- [21] Mitchell, N. P., Nash, L. M. & Irvine, W. T. M. Realization of a topological phase transition in a gyroscopic lattice. *Phys. Rev. B* **97**, 100302 (2018).
- [22] Nonetheless, the interaction conserves linear momentum because the forces on the two participating masses are equal and opposite.
- [23] Nash, L. M. *et al.* Topological mechanics of gyroscopic metamaterials. *Proc. Natl. Acad. Sci. USA* **112**, 14495–500 (2015).
- [24] Wang, P., Lu, L. & Bertoldi, K. Topological Phononic Crystals with One-Way Elastic Edge Waves. *Physical review letters* **115**, 104302 (2015).
- [25] Souslov, A., van Zuiden, B. C., Bartolo, D. & Vitelli, V. Topological sound in active-liquid metamaterials. *Nature Physics* **13**, 1091 (2017).
- [26] Hatano, N. & Nelson, D. R. Localization transitions in non-hermitian quantum mechanics. *Phys. Rev. Lett.* **77**, 570–573 (1996).
- [27] Bender, C. M. & Boettcher, S. Real spectra in non-hermitian hamiltonians having pt symmetry. *Phys. Rev. Lett.* **80**, 5243–5246 (1998).
- [28] Wang, Y.-X. & Clerk, A. A. Non-hermitian dynamics without dissipation in quantum systems. *Phys. Rev. A* **99**, 063834 (2019).
- [29] Hasan, M. Z. & Kane, C. L. Colloquium: Topological insulators. *Rev. Mod. Phys.* **82**, 3045–3067 (2010).
- [30] Sone, K., Ashida, Y. & Sagawa, T. Exceptional non-hermitian topological edge mode and its application to active matter (2019). arXiv:1912.09055.
- [31] Kawabata, K., Bessho, T. & Sato, M. Classification of exceptional points and non-hermitian topological semimetals. *Phys. Rev. Lett.* **123**, 066405 (2019).
- [32] Zhou, H., Lee, J. Y., Liu, S. & Zhen, B. Exceptional surfaces in pt -symmetric non-hermitian photonic systems. *Optica* **6**, 190–193 (2019).
- [33] Ghatak, A. & Das, T. New topological invariants in non-hermitian systems. *Journal of Physics: Condensed Matter* **31**, 263001 (2019).
- [34] Heiss, W. The physics of exceptional points. *Journal of Physics A: Mathematical and Theoretical* **45**, 444016 (2012).
- [35] Shen, H., Zhen, B. & Fu, L. Topological band theory for non-hermitian hamiltonians. *Phys. Rev. Lett.* **120**, 146402 (2018).
- [36] Lau, H.-K. & Clerk, A. A. Fundamental limits and non-reciprocal approaches in non-hermitian quantum sensing. *Nature Communications* **9**, 4320 (2018).
- [37] Berry, M. V. Quantal phase factors accompanying adiabatic changes. *Proceedings of the Royal Society of London. A. Mathematical and Physical Sciences* **392**, 45–57 (1984).
- [38] Yao, S., Song, F. & Wang, Z. Non-hermitian chern bands. *Phys. Rev. Lett.* **121**, 136802 (2018).
- [39] Poli, C., Bellec, M., Kuhl, U., Mortessagne, F. & Schomerus, H. Selective enhancement of topologically induced interface states. *Nature Communications* **6**, 4 (2014). 1407.3703.
- [40] Kunst, F. K. & Dwivedi, V. Non-hermitian systems and topology: A transfer-matrix perspective. *Phys. Rev. B* **99**, 245116 (2019).
- [41] Torres, L. E. F. F. Perspective on topological states of non-hermitian lattices. *Journal of Physics: Materials* **3**, 014002 (2019).
- [42] Li, L., Lee, C. H. & Gong, J. Geometric characterization of non-hermitian topological systems through the singularity ring in pseudospin vector space. *Phys. Rev. B* **100**, 075403 (2019).
- [43] Herviou, L., Bardarson, J. H. & Regnault, N. Defining a bulk-edge correspondence for non-hermitian hamiltonians via singular-value decomposition. *Phys. Rev. A* **99**, 052118 (2019).
- [44] Kawabata, K., Shiozaki, K., Ueda, M. & Sato, M. Symmetry and topology in non-hermitian physics. *Phys. Rev. X* **9**, 041015 (2019).
- [45] Gong, Z. *et al.* Topological phases of non-hermitian systems. *Phys. Rev. X* **8**, 031079 (2018).
- [46] Kawabata, K., Higashikawa, S., Gong, Z., Ashida, Y. & Ueda, M. Topological unification of time-reversal and particle-hole symmetries in non-hermitian physics. *Nature Communications* **10**, 297 (2019).
- [47] Longhi, S. Topological phase transition in non-hermitian quasicrystals. *Phys. Rev. Lett.* **122**, 237601 (2019).
- [48] Yao, S. & Wang, Z. Edge states and topological invariants of non-hermitian systems. *Phys. Rev. Lett.* **121**, 086803 (2018).
- [49] Fei Song, S. Y. & Wang, Z. Non-hermitian skin effect and chiral damping in open quantum systems (2019). arXiv:1904.08432v1.
- [50] Yuce, C. Non-hermitian anomalous skin effect (2019). arXiv:1905.09328v1.
- [51] Lee, C. H. & Thoma, R. Anatomy of skin modes and topology in non-hermitian systems. *Phys. Rev. B* **99**, 201103 (2019).
- [52] Xiong, Y. Why does bulk boundary correspondence fail in some non-hermitian topological models. *Journal of Physics Communications* **2**, 035043 (2018).
- [53] Li, M., Ni, X., Weiner, M., Alù, A. & Khanikaev, A. B. Topological phases and nonreciprocal edge states in non-hermitian floquet insulators. *Phys. Rev. B* **100**, 045423 (2019).
- [54] Sounas, D. L. & Alu, A. Non-reciprocal photonics based on time modulation. *Nature Photonics* **11**, 774 (2017).
- [55] Prodan, E. & Prodan, C. Topological phonon modes and their role in dynamic instability of microtubules. *Physical Review Letters* **103**, 248101 (2009).
- [56] Chen, W. & Schnyder, A. P. Universality classes of topological phase transitions with higher-order band crossing. *New Journal of Physics* **21**, 073003 (2019).
- [57] Haldane, F. D. M. Model for a Quantum Hall Effect without Landau Levels: Condensed-Matter Realization of the “Parity Anomaly”. *Physical Review Letters* **61**, 2015–2018 (1988).
- [58] Mitchell, N. P., Nash, L. M., Hexner, D., Turner, A. & Irvine, W. T. M. Amorphous gyroscopic topological metamaterials (2016). arXiv:1612.09267.

- [59] Mitchell, N. P., Nash, L. M., Hexner, D., Turner, A. M. & Irvine, W. T. M. Amorphous topological insulators constructed from random point sets. *Nature Physics* **14**, 380–385 (2018).
- [60] Fruchart, M. & Carpentier, D. An introduction to topological insulators. *Comptes Rendus Physique* **14**, 779 – 815 (2013). Topological insulators / Isolants topologiques.
- [61] Fukui, T., Hatsugai, Y. & Suzuki, H. Chern Numbers in Discretized Brillouin Zone: Efficient Method of Computing (Spin) Hall Conductances. *Journal of the Physical Society of Japan* (2013).